

# Rapid Vision-based Shape and Motion Analysis System for Fast-flowing Cells in a Microchannel

Qingyi Gu, Tadayoshi Aoyama, Takeshi Takaki, and Idaku Ishii

**Abstract**—This paper proposes a novel method for simultaneous cell shape and motion analysis in rapid microchannel flows based on a multi-object feature extraction algorithm with a frame-straddling high-speed vision platform. This system can synchronize two camera inputs that share the same view with only a very small sub-microsecond time delay. Real-time video processing is performed using the hardware logic by extracting the moment features of multiple cells at 2000 fps or more, which are obtained from the two camera inputs, and their frame-straddling time can be adjusted from 0 to 0.5 ms in 9.9 ns steps. After setting the frame-straddling time within a certain range to avoid large image displacements between the two camera inputs, the frame-straddling high-speed vision platform can perform simultaneous shape and motion analysis of cells in fast microchannel flows of 1 m/s or greater. The results of real-time experiments conducted to analyze the deformabilities, velocities, and shapes of fast-flowing sea urchin egg cells in straight and L-type microchannels verified the efficacy of our vision-based cell analysis system.

## I. INTRODUCTION

Recent progress in micrometer-scale techniques has facilitated the analysis of cells using a lab-on-a-chip (LOC) [1]. LOC is a high-throughput device that integrates laboratory functions on a single chip measuring a few square centimeters or less, which contains a microfluidic network of microchannels. Several non-vision-based cell analysis systems have been developed to extract the shapes and motions of cells in LOCs [2]. However, the detectable geometrical properties of cells have been limited by several technical factors, such as poor spatial resolution and the difficulty of obtaining quantitative measurements at such small scales. To overcome these constraints, vision-based cell analysis systems have been proposed for analyzing the shapes and motions of cells in microchannel flows, such as red blood cells (RBCs) and cancer cells.

Real-time vision-based shape analysis systems for cells in microchannels are being developed for many biological applications [3], [4]. However, the frame rates of most of these systems are limited by conventional video signals (NTSC: 30 fps, PAL: 25 fps), which are not sufficiently fast to allow the observation of cells flowing in microchannels. Offline high-speed cameras have recently been used for vision-based cell analysis in microchannel flows [5], [6]. However, the measurement speed of cells flowing in microchannels is often limited by the frame intervals of the offline high-speed cameras, because the apparent speed of the microchannel flow increases in microscopic views as the magnification ratio becomes larger. To improve the speed that can be measured without increasing the frame rate of a

vision system, a frame-straddling technique that used a pair of images with a microsecond time delay has been applied to an online particle image velocimetry (PIV) system [7]. If this frame-straddling function could be applied to a real-time multi-object feature extraction system, it would significantly improve the upper limit of the measurement speed for online cell shape and motion analysis in microchannels.

Recently, field-programmable gate array (FPGA)-based high-speed vision platforms have been developed for hardware implementations of various types of image processing algorithms. Gu et al. developed a multi-object feature extraction system for rapid shape-based blob processing, which could extract multiple objects and their shape features in real time using  $512 \times 512$  images at 2000 fps [8]. The use of a real-time function to measure the shapes and speeds of multiple objects could accelerate microchannel-based cell analysis of the shape, motion, stiffness, and other image-based parameters, thereby facilitating the automated mass production of cells.

In the present study, we propose a real-time cell shape and motion analysis system for inspecting fast-flowing cells in microchannels, which is based on a frame-straddling high-speed vision platform. The system uses two camera inputs and a frame-straddling function. It has a time delay that ranges from 0 to 0.5 ms in 9.9 ns steps, which can avoid large image displacements between the two camera inputs when observing fast-flowing cells. Thus, our system facilitates cell shape inspection in microchannel flows at 1 m/s or greater based on real-time video processing with multi-object feature extraction using  $512 \times 256$  images at 4000 fps, or  $512 \times 512$  images at 2000 fps, where the images are obtained from two camera inputs and there is only a very small time delay.

## II. CELL SHAPE AND MOTION ANALYSIS SYSTEM BASED ON FRAME-STRADDLING HIGH-SPEED VISION

### A. Concept

We introduce the concept of frame-straddling multi-object feature extraction for measuring the shapes and speeds of cells in microchannel flows simultaneously. Figure 1 shows an outline of the system used for microchannel-based cell shape and motion analysis. Given a frame-straddling high-speed vision system that can synchronize two camera inputs of the same view field with a time delay, which can obtain the positions, sizes, and other features of multiple objects in images at a high frame rate, the time delay can be adjusted in a suitable range for specific processes to calculate the speeds of cells flowing in microchannels, thereby avoiding large image displacements between the two camera inputs. Compared with a single-camera system, our frame-straddling concept can expand the measurable range of speeds for fast-flowing cells in microchannels to 1 m/s or more, without

Q. Gu, T. Aoyama, T. Takaki, and I. Ishii are with the Department of System Cybernetics, Hiroshima University, 1-4-1, Kagamiyama, Higashi-Hiroshima, Hiroshima 739-8527, Japan. Email: gu@robotics.hiroshima-u.ac.jp

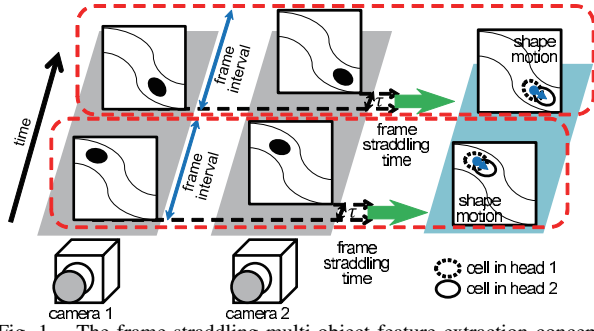


Fig. 1. The frame-straddling multi-object feature extraction concept.

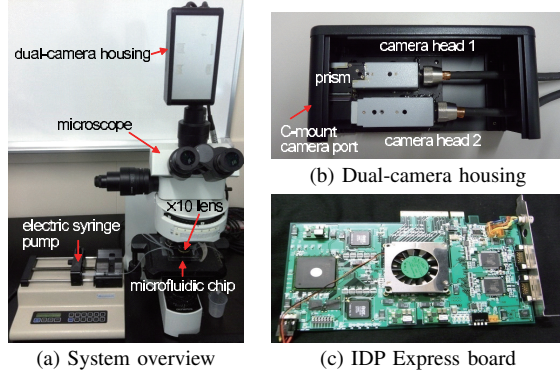


Fig. 2. System overview.

increasing the frame rate and the computational cost of the vision system. The shape deformation of fast-flowing cells in microchannels can also be quantified in real time to facilitate the long-term automated sorting of cells in LOCs.

### B. System Configuration

We propose a fast vision-based shape and motion analysis system for fast-flowing cells in microchannels based on a hardware implementation of a cell-based multi-object feature extraction algorithm [8] using a dual-camera high-speed vision platform, as shown in Fig. 2(a). Our system comprises a dual-camera high-speed vision platform (IDP Express) [9] with a frame-straddling function for two camera inputs, a microscope (BX51RT; Olympus Co., Tokyo, Japan), a metal-halide light source (PCS-MH375RC; Optical Garden Co., Tokyo, Japan), microfluidic chips with microchannels that measure hundreds of micrometers in width, and an electric syringe pump (KDS200; KD Scientific Inc., Holliston, MA, USA). The camera housing shown in Fig. 2(b), where the two camera heads of the IDP Express system are arranged so they can capture a common view via a prism, is mounted on top of the camera port of the BX51RT microscope. In the present study, the microchannels on the microfluidic chips were observed using a 10 $\times$  objective lens, where the measured area was 512 $\times$ 512  $\mu\text{m}$  and one pixel corresponded to 1.0  $\mu\text{m}$  in the microscopic view of 512 $\times$ 512 pixels on a 10  $\mu\text{m}$ -pixel-pitch image sensor.

The IDP Express board has two camera inputs, an FPGA for camera I/O and PCI-e bus controls, a user-specified FPGA (Xilinx XC3S5000) for the hardware implementation of the algorithms, and several peripheral I/O circuits. Figure 2(c) shows an overview of the board. The details of the image processing path and transfer in the IDP Express

board were described in a previous study [9]. In the present study, the input images from two camera heads are processed simultaneously at 2000 fps or more by implementing the cell-based multi-object feature extraction algorithm [8] in the hardware logic of the user-specified FPGA. In addition, the IDP Express board is customized for dual-camera frame-straddling by improving the hardware logic of the time delay control between the two camera heads. The time delay between the two camera heads is controlled simultaneously via the PC from 0 to 0.5 ms in 9.9-ns steps. The input images of the two camera heads and the processed results on the IDP Express board are memory-mapped via eight-lane PCI-e buses at 2000 fps or more onto the allocated memory in the PC with an ASUSTek P6T7 mainboard, Intel Core i7 975 3.33 GHz CPU, 6 GB memory, 4 $\times$ PCI-e 2.0 $\times$ 16 buses I/F, and the Windows XP Professional 32-bit OS. Arbitrary processing can be programmed to allow real-time execution on the PC.

### C. Algorithms

To facilitate the real-time shape and motion analysis of  $L$  cells flowing in microchannels, we implemented the following algorithms for a pair of frame-straddled  $M \times N$  images: (1) offline pre-processing for dual-camera calibration; (2) feature extraction from multiple cells in microchannels; and (3) motion estimation based on cell tracking using a pair of frame-straddled images.

#### (1) Pre-processing for dual-camera calibration

##### a) Calculation of the brightness ratio

To adjust the brightness difference between the two camera inputs, the brightness ratio  $R_{12}$  is determined by calculating the total image brightness as follows:

$$R_{12} = \frac{\sum_{x,y} {}^2I_R(x,y)}{\sum_{x,y} {}^1I_R(x,y)}, \quad (1)$$

where  ${}^1I_R(x,y)$  and  ${}^2I_R(x,y)$  are the reference images at pixel  $(x,y)$  in camera heads 1 and 2, respectively, when a non-saturated bright scene is captured with no time delay between the two camera inputs.

##### b) Calculation of the affine parameters

To adjust the geometric differences between the two camera inputs, the image coordinates of camera head 1 are calibrated based on those of camera head 2 using an affine transformation as follows:

$$\begin{pmatrix} x' \\ y' \end{pmatrix} = \begin{pmatrix} a_{11} & a_{12} \\ a_{21} & a_{22} \end{pmatrix} \begin{pmatrix} x \\ y \end{pmatrix} + \begin{pmatrix} b_1 \\ b_2 \end{pmatrix}. \quad (2)$$

where  $(x',y')$  are the image coordinates of camera head 1 after calibration, while  $a_{11}, a_{12}, a_{21}, a_{22}, b_1$ , and  $b_2$  are the affine parameters, which indicate the geometric relationships between the image coordinates of camera heads 1 and 2. These affine parameters are obtained using images captured when a 30- $\mu\text{m}$ -pitch micro-chess pattern is observed with no time delay between the two camera inputs, in the same manner as the widely used camera calibration method [10].

##### c) Assignment of microchannel regions

To avoid confusing the cell regions with the microchannel walls during image binarization, the following one-bit mask images  ${}^iC(x, y)$  ( $i = 1, 2$ ) are preassigned as the inner regions of the microchannels that need to be observed as the two camera inputs:

$${}^iC(x, y) = \begin{cases} 1 & ((x, y) \text{ belongs to inner region}) \\ 0 & (\text{otherwise}) \end{cases}, \quad (3)$$

where the assignments are made when the microchannels are observed in the same conditions used in the online experiments, except there are no cells in the microchannels.

## (2) Feature extraction from multiple cells

### a) Binarization of input images

The input image of the camera head  $i$  ( $i = 1, 2$ ) captured at time  $t$ ,  ${}^iI(x, y, t)$ , is converted into a binary image  ${}^iB(x, y, t)$  using its corresponding mask image  ${}^iC(x, y)$ , as follows:

$${}^iB(x, y, t) = \begin{cases} {}^iC(x, y) & ({}^iI(x, y, t) \leq {}^i\theta_B) \\ 0 & (\text{otherwise}) \end{cases}, \quad (4)$$

where the threshold  ${}^i\theta_B$  is determined using a specific value  $\theta_B$  and the brightness ratio  $R_{12}$  is as follows:

$${}^1\theta_B = \theta_B, \quad {}^2\theta_B = R_{12} \cdot \theta_B. \quad (5)$$

### b) Calculation of subregion-based moment features

The zeroth-, first-, and second-order moment features are calculated for  $M'N'$  subregions  $\Gamma_{ab}$  ( $a = 0, \dots, M' - 1, b = 0, \dots, N' - 1$ ) with  $m \times n$  pixels in  ${}^iB(x, y, t)$  as follows:

$${}^iM_{pq}(\Gamma_{ab}, t) = \sum_{x=am}^{a(m+1)-1} \sum_{y=bn}^{b(n+1)-1} x^p y^q \cdot {}^iB(x, y, t), \quad (6)$$

where  $M = mM'$  and  $N = nN'$ ; and  $p$  and  $q$  are non-negative integers that satisfy  $p + q \leq 2$ .  $\Gamma_{ab}$  is expressed as follows:

$$\Gamma_{ab} = \{(x, y) | (am + s, bn + t), 0 \leq s < m, 0 \leq t < n\}. \quad (7)$$

### c) Labeling of connected components with feature calculations

To obtain the moment features of multiple objects in an image, the connected components labeling process is accelerated using the cell-based labeling algorithm with the moment features for  $M'N'$  subregions,  ${}^iM_{pq}(\Gamma_{ab}, t)$  [11]. The computational complexity and memory consumption of the labeling process can be reduced by the order of  $O(M'N')$ , i.e.,  $1/mn$  of the pixel-level complexity of the order  $O(MN)$ . For labeled objects  ${}^iO_l(t)$  ( $l = 0, \dots, L - 1$ ) in  ${}^iB(x, y, t)$ , the label-domain moment features  $M_{pq}({}^iO_l(t))$  ( $p + q \leq 2$ ) are accumulated sequentially, at the same time as the scanning of a flag map  ${}^iP_{ab}(t)$  with  $M' \times N'$  subregions.  ${}^iP_{ab}(t)$  is defined by checking  ${}^iM_{00}(\Gamma_{ab}, t)$  with a threshold  $\theta_P$ , as follows:

$${}^iP_{ab}(t) = \begin{cases} 1 & ({}^iM_{00}(\Gamma_{ab}, t) \geq \theta_P) \\ 0 & (\text{otherwise}) \end{cases}, \quad (8)$$

where  $M_{pq}({}^iO_l(t))$  are defined as follows:

$$M_{pq}({}^iO_l(t)) = \sum_{(x, y) \in {}^iO_l(t)} x^p y^q \cdot {}^iB(x, y, t). \quad (9)$$

The detailed processes used to calculate the label-domain moment features in an image are given in [8] and [11].

Using the zeroth-, first-, and second-order label-domain moment features, the sizes  $S({}^iO_l(t))$ , centroid positions  $\mathbf{X}({}^iO_l(t))$ , and eccentricities  $E({}^iO_l(t))$  are calculated for  $L$  labeled objects  ${}^iO_l(t)$  in  ${}^iB(x, y, t)$ , as follows:

$$S({}^iO_l(t)) = M_{00}({}^iO_l(t)), \quad (10)$$

$$\begin{aligned} \mathbf{X}({}^iO_l(t)) &= (X({}^iO_l(t)), Y({}^iO_l(t))) \\ &= \left( \frac{M_{10}({}^iO_l(t))}{M_{00}({}^iO_l(t))}, \frac{M_{01}({}^iO_l(t))}{M_{00}({}^iO_l(t))} \right), \end{aligned} \quad (11)$$

$$E({}^iO_l(t)) = \frac{\lambda^+({}^iO_l(t)) - \lambda^-({}^iO_l(t))}{\lambda^+({}^iO_l(t)) + \lambda^-({}^iO_l(t))}, \quad (12)$$

where  $e_{20}({}^iO_l(t))$ ,  $e_{11}({}^iO_l(t))$ , and  $e_{02}({}^iO_l(t))$  are the second-order moment features about the centroid position for  ${}^iO_l(t)$ . The eccentricity  $E({}^iO_l(t))$  is expressed using the major axis  $\lambda^+({}^iO_l(t))$  and the minor axis  $\lambda^-({}^iO_l(t))$ , where  ${}^iO_l(t)$  is approximated as an ellipse, which indicates the degree of deviation from a true circle.  $\lambda^+({}^iO_l(t))$ ,  $\lambda^-({}^iO_l(t))$ ,  $e_{20}({}^iO_l(t))$ ,  $e_{11}({}^iO_l(t))$ , and  $e_{02}({}^iO_l(t))$  are calculated as follows:

$$e_{20}({}^iO_l(t)) = \frac{M_{20}({}^iO_l(t))}{M_{00}({}^iO_l(t))} - (X({}^iO_l(t)))^2, \quad (13)$$

$$e_{11}({}^iO_l(t)) = \frac{M_{11}({}^iO_l(t))}{M_{00}({}^iO_l(t))} - X({}^iO_l(t))Y({}^iO_l(t)), \quad (14)$$

$$e_{02}({}^iO_l(t)) = \frac{M_{02}({}^iO_l(t))}{M_{00}({}^iO_l(t))} - (Y({}^iO_l(t)))^2, \quad (15)$$

$$\lambda^+({}^iO_l(t)) = e_{20} + e_{02} + \sqrt{4(e_{11})^2 + (e_{20} - e_{02})^2}, \quad (16)$$

$$\lambda^-({}^iO_l(t)) = e_{20} + e_{02} - \sqrt{4(e_{11})^2 + (e_{20} - e_{02})^2}. \quad (17)$$

These shape parameters are calculated for  $L$  labeled objects  ${}^iO_l$  in  ${}^iB(x, y, t)$  ( $i = 1, 2$ ) using both camera inputs.

## (3) Cell tracking for motion estimation

### a) Cell sorting in the flow direction

When the sizes of the labeled objects exceed a specific threshold,  $\theta_S$ , the labeled objects are sorted in the upstream direction of the microchannel, as follows:

$${}^i\tilde{O}_u(t) = \text{sort}({}^i\mathcal{F}(t), u) \quad (u = 1, \dots, U(t)), \quad (18)$$

$${}^i\mathcal{F}(t) = \{ {}^iO_l(t) : S({}^iO_l(t)) > \theta_S \quad (l = 1, \dots, L) \}, \quad (19)$$

where  ${}^i\tilde{O}_u(t)$  is the  $u$ -th farthest object from the upstream end of the microchannel in an image, which belongs to a set  ${}^i\mathcal{F}(t)$ . Its centroid position  ${}^i\mathbf{X}({}^i\tilde{O}_u)$  satisfies the following condition:

$$d({}^i\tilde{O}_{u_1}(t)) \geq d({}^i\tilde{O}_{u_2}(t)) \quad \text{when } u_1 \leq u_2, \quad (20)$$

$$d({}^i\tilde{O}_u(t)) = |\mathbf{X}({}^i\tilde{O}_u(t)) - \mathbf{X}_U|, \quad (21)$$

where  $\mathbf{X}_U = (X_U, Y_U)$  are the  $x, y$  coordinates of the upstream end of the microchannel in an image.

### b) Velocity calculation using frame-straddled images

To match the sorted objects as cell regions in the two camera inputs, the displacement  $\mathbf{V}_{uu'}(t)$  between  ${}^1\tilde{O}_{u'}(t - \tau)$  and  ${}^2\tilde{O}_u(t)$  is calculated as follows:

$$\begin{aligned} \mathbf{V}_{uu'}(t) &= \mathbf{X}({}^2\tilde{O}_u(t)) - \hat{\mathbf{X}}({}^1\tilde{O}_{u'}(t - \tau)) \\ &\quad (u' = 1, \dots, U(t - \tau), u = 1, \dots, U(t)), \end{aligned} \quad (22)$$

where  $\tau$  is the frame-straddling time difference between the two camera inputs. In this case,  $\mathbf{V}_{uu'}(t)$  is expressed as the image coordinates of camera head 2 and the centroid position of  ${}^1\tilde{O}_{u'}(t-\tau)$  is calibrated using the initial affine parameters as follows:

$$\hat{\mathbf{X}}({}^1O_{u'}(t-\tau)) = \begin{pmatrix} a_{11} & a_{12} \\ a_{21} & a_{22} \end{pmatrix} \mathbf{X}({}^1O_{u'}(t-\tau)) + \begin{pmatrix} b_1 \\ b_2 \end{pmatrix}. \quad (23)$$

Assuming that  $\tau$  is so small that the cell displacements are minimal between the two frame-straddled images, the  $u$ -th cell region  ${}^2\tilde{O}_u(t)$  in the view of camera head 2 corresponds to its nearest cell region  ${}^1\tilde{O}_{u'_M(u)}(t-\tau)$  in the view of camera head 1 if their displacement is less than a specific threshold  $\theta_V$ , where its object number  $u'_M(u)$  is determined as follows.

$$u'_M(u) = \begin{cases} \arg \min_{u'} |\mathbf{V}_{uu'}(t)| & (\min |\mathbf{V}_{uu'}(t)| < \theta_V) \\ \emptyset & (\text{otherwise}) \end{cases}, \quad (24)$$

The velocity of the  $u$ -th cell region  $\mathbf{v}({}^2\tilde{O}_u(t))$  in the view of camera head 2 is calculated as the displacement magnified by the reciprocal of the frame-straddling time as follows:

$$\mathbf{v}({}^2\tilde{O}_u(t)) = \frac{1}{\tau} \mathbf{V}_{uu'_M(u)}(t). \quad (25)$$

### c) Tracking identified cells

In general, the cells flowing in microchannels are observed in many frames of a single camera input, because the observation time depends on their speeds. To avoid the incorrect counting of the same cells as different cells, all of the cell regions  ${}^2\tilde{O}_u(t)$  ( $u = 1, \dots, U(t)$ ) in the view of camera head 2 at current time  $t$  are tracked by matching them with those at the previous time  $t - \Delta t$ .  $\Delta t$  is the frame interval of the input images for camera head 2. Assuming that the cells flow unidirectionally in the microchannels and move further from the upstream end as time passes, their identification numbers are assigned in ascending order of  $l'$ , i.e., in order of their distance from the upstream end.

If there are cell regions at time  $t - \Delta t$  in the upstream region from the  $u$ -th cell region  ${}^2\tilde{O}_u(t)$  at time  $t$  that do not correspond with the cell regions  ${}^2\tilde{O}_1(t), \dots, {}^2\tilde{O}_{u-1}(t)$  at time  $t$ ,  ${}^2\tilde{O}_u(t)$  corresponds to the farthest cell region from the upstream end of the cell regions at time  $t - \Delta t$  in the upstream region. For  $u = 1, \dots, U(t)$ , its identification number  $Q({}^2\tilde{O}_u(t))$  is assigned as follows:

$$Q({}^2\tilde{O}_u(t)) = Q({}^2\tilde{O}_{u'_T(u)}(t - \Delta t)) \quad (u = 1, \dots, U(t)), \quad (26)$$

$$u'_T(u) = \min u', \quad (27)$$

$$\text{s.t. } d({}^2\tilde{O}_u(t)) \geq d({}^2\tilde{O}_{u'}(t - \Delta t)) \quad (28)$$

$$\text{and } u'_T(u-1) < u' \leq U(t - \Delta t), \quad (29)$$

where the order of the cell regions at time  $t$  is preserved in the order of their corresponding objects at time  $t - \Delta t$ ;  $u'_T(u_1) > u'_T(u_2)$  when  $u_1 > u_2$ . Initially,  $u'_T(u)$  is set to zero when  $u = 1$ .

Otherwise,  ${}^2\tilde{O}_u(t)$  is regarded as a new cell region in the image and its identification number  $Q({}^2\tilde{O}_u(t))$  is assigned a new number, which is the minimum number of those that have not been assigned to any cell regions.

After the tracking process, the moment-based shape features and velocities described in Eqs (10)–(12) and (25)

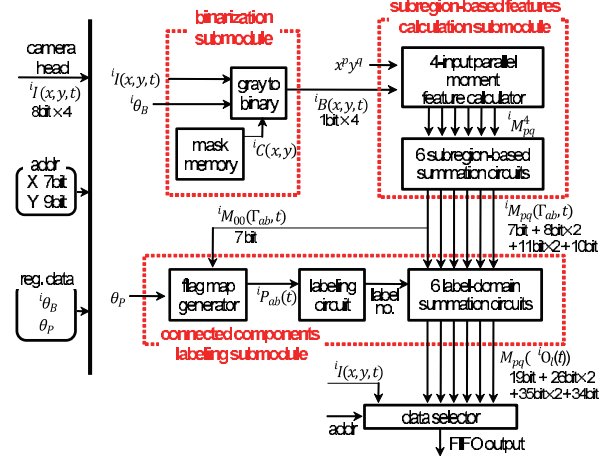


Fig. 3. Schematic showing the data flow.

are assigned to all of the identified cell regions, and these features facilitate the analysis of the motion and shapes of the cells flowing in the microchannels.

### D. Implementation of the Hardware Logic and its Specification

The process used to extract the features from multiple cells, which has a computational complexity of  $O(MN)$ , was implemented in the hardware logic of the user-specified FPGA on the IDP Express board. Figure 3 shows a schematic of the data flow of the multi-object moment feature extraction module implementation, which was designed as an extended multi-object feature extraction circuit [8] to facilitate the rapid analysis of cells flowing in microchannels. The system comprises a binarization submodule, a subregion-based features calculation submodule, a connected components labeling submodule, and a data selector for the FIFO output. The input images obtained from camera heads 1 and 2 are scanned in parallel with a time delay  $\tau$  to allow frame-straddling. The input images from each camera head are scanned in units of four pixels from the upper left to the lower right using  $X$  and  $Y$  address signals with a 151.2 MHz clock. In the present study, the two circuit modules shown in Fig. 3 were implemented to allow the parallel execution of multi-object moment feature extraction based on the two camera inputs. The delay time when calculating the label-domain moment features of 512 labeled objects is 25 clocks (one clock = 6.6 ns) after raster-scanning all of the pixels in an input image, while the delay time when outputting them to the external PC is one frame.

## III. EXPERIMENTS

To verify the performance of our vision-based cell analysis system, we conducted two experiments using sea urchin egg cells that flowed in straight and L-type microchannels, which were fabricated from polydimethylsiloxane and had a rectangular cross-section that measured 200  $\mu\text{m}$  wide and 100  $\mu\text{m}$  deep. In the experiments, water containing sea urchin egg cells (*Hemicentrotus pulcherrimus*) that measured 80–100  $\mu\text{m}$  in diameter was injected into the microchannel using an electric syringe pump. After dual-camera calibration, the affine parameters were set to  $a_{11} = 1.000$ ,  $a_{12} = 0.001$ ,  $a_{21} = -0.001$ ,  $a_{22} = 0.999$ ,  $b_1 = -2.66$ , and  $b_2 = 0.19$ . The

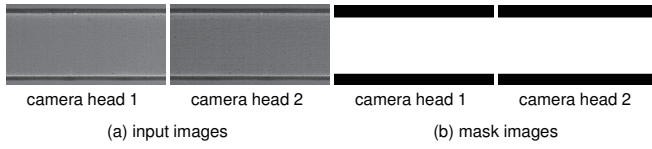


Fig. 4. Input and mask images used for the straight microchannel.

TABLE I

TIME DURATIONS AND NUMBER OF CELLS COUNTED FOR SEA URCHIN EGG CELLS AT DIFFERENT FLOW RATES.

flow rate [ $\mu\text{l}/\text{min}$ ]	125	250	500	1000	2000
time duration [s]	96.4	61.6	58.8	32.4	24.7

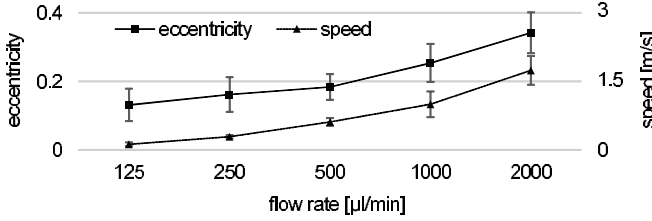


Fig. 5. Speeds and eccentricities of sea urchin egg cells at different flow rates in a straight microchannel.

exposure times of the two camera heads were  $6.25 \mu\text{s}$ . The threshold used to determine active subregions was set to  $\theta_P = 4$ , the threshold used to reject small labeled objects was set to  $\theta_S = 7000$ , and the threshold used to determine corresponding objects in two frame-straddled images was set to  $\theta_V = 80$ .

#### A. Sea urchin egg cells flowing in a straight microchannel

The experiment used sea urchin egg cells spawned on the previous day, which flowed from left to right in a straight microchannel, where the upstream end of the microchannel was set to  $X_U = (0, 128)$ . The brightness ratio was set to  $R_{12} = 0.83$ . The mask images of the two camera inputs,  ${}^1C(x, y)$  and  ${}^2C(x, y)$ , were prestored, as shown in Fig. 4. The threshold for binarization was set to  $\theta_B = 69$ . The  $512 \times 256$  input images and label-domain features were recorded in real time at 2000 fps for data logging whereas the label-domain features of  $512 \times 256$  input images were extracted at 4000 fps.

The sea urchin egg cells were subjected to different flow speed and were observed to quantify the deformation of their shapes with rapid microchannel flow rates. The frame-straddling times were set to  $\tau = 240, 240, 80, 40$ , and  $20 \mu\text{s}$ , when the flow rates were 125, 250, 500, 1000, and 2000  $\mu\text{l}/\text{min}$ , respectively. Measurements were acquired continuously during each trial with different flow rates, except when the number of cells counted exceeded 800. Table I shows the time durations and the number of cells counted in the trials at different flow rates.

Figure 5 shows the averages and standard deviations for the speeds and eccentricities of the egg cells at flow rates of 125, 250, 500, 1000, and 2000  $\mu\text{l}/\text{min}$ . The average speed of the egg cells increased by 0.12, 0.28, 0.60, 0.97, and 1.70 m/s as the flow rate increased to 125, 250, 500, 1000, and 2000  $\mu\text{l}/\text{min}$ , respectively. This demonstrated that our system could observe sea urchin egg cells with rapid flow rates of 1 m/s or more in the microchannels, which corresponded to an image

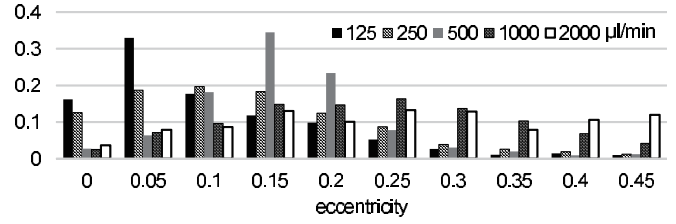


Fig. 6. Eccentricity histograms for sea urchin egg cells at different flow rates in a straight microchannel.

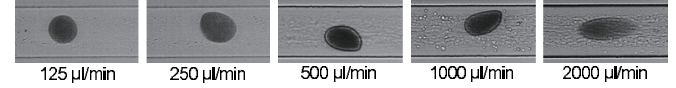


Fig. 7. Snapshots of sea urchin egg cells at different flow rates in a straight microchannel.

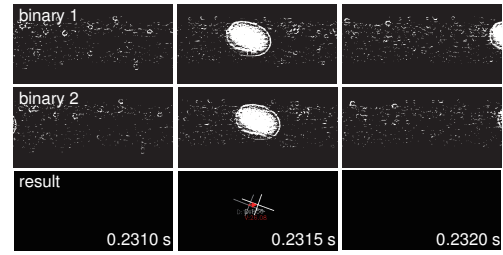


Fig. 8. Binarized images,  $x, y$  positions, and velocities of a tracked sea urchin egg cell flowing in a straight microchannel at 1000  $\mu\text{l}/\text{min}$ .

displacement of  $1 \times 10^6$  pixels or more per second in the microscopic view.

Figure 6 shows the relative eccentricity histograms for the egg cells flowing at different speeds, where the bin size is 0.05. Figure 7 shows snapshots of the egg cells. The average eccentricities of the egg cells increased by 0.13, 0.16, 0.18, 0.25, and 0.34 as the flow rate increased to 125, 250, 500, 1000, and 2000  $\mu\text{l}/\text{min}$ , respectively. This trend corresponded to the degree of sea urchin egg cell shape deformation shown in Fig. 7, where the egg cells became more deformed as the flow rate increased.

Figure 8 shows three binarized image sequences obtained from the two camera heads, their  $x, y$  positions, and the velocity of the tracked egg cell, which were taken at intervals of 0.5 ms for  $t = 0.2310$ – $0.2320$  s. In the figure, the  $x, y$  positions of the same egg cell are shown at different times based on the two camera inputs with the major axes and minor axes, where the egg cell was approximated as an ellipse in the image coordinates from camera head 2. In Fig. 8, the egg cell was only observed in one or two frames in the image sequence at 2000 fps, which made it difficult to estimate its velocity from a single camera view. However, the egg cell was observed without large image displacements between the two camera views by setting their frame-straddling time to  $40 \mu\text{s}$ , i.e.,  $40 \mu\text{s}$  is 0.08 times 0.5 ms, which was the frame interval for the 2000 fps video. This demonstrated that our system could measure the motion and shapes of the cells in the microchannel simultaneously using two frame-straddled camera inputs with a small time delay, even when the cells flowed too rapidly to be tracked in a single camera view.



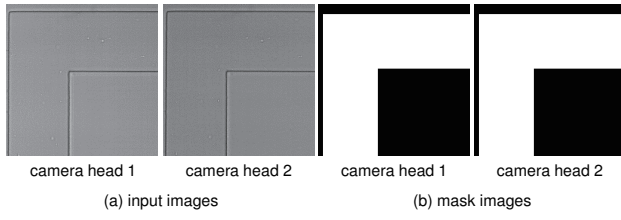


Fig. 9. Input and mask images for an L-type microchannel.

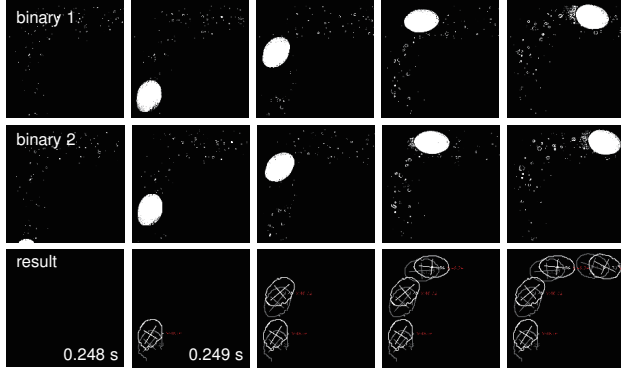


Fig. 10. Binarized images,  $x, y$  positions, velocities, and contours of a tracked sea urchin egg cell flowing in an L-type microchannel at 250  $\mu\text{l}/\text{min}$ .

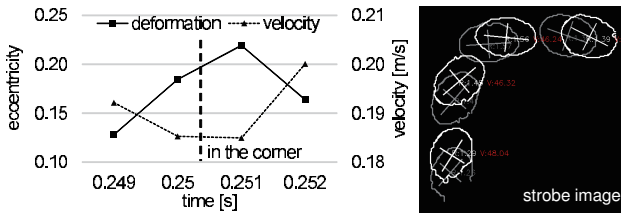


Fig. 11. Eccentricities and velocities of sea urchin eggs flowing in an L-type microchannel at 250  $\mu\text{l}/\text{min}$ .

### B. Sea urchin egg cells flowing in an L-type microchannel

In this experiment, one-day-old sea urchin egg cells flowed from the left bottom to the right top of an L-type microchannel, where the upstream end of the microchannel was set to  $X_U = (0, 511)$ . The brightness ratio was set to  $R_{12} = 0.83$ . The mask images used for the two camera inputs,  ${}^1C(x, y)$  and  ${}^2C(x, y)$ , were prestored, as shown in Fig. 9. The threshold for binarization was set to  $\theta_B = 60$ . The  $512 \times 512$  input images and label-domain features were recorded in real time at 1000 fps to allow data logging whereas the label-domain features of  $512 \times 512$  input images were extracted at 2000 fps.

Sea urchin egg cells were observed flowing in a L-type microchannel at 250  $\mu\text{l}/\text{min}$  to quantify the deformation of their shapes in irregular microchannel, where the frame-straddling time was set to  $\tau = 250 \mu\text{s}$ . Figure 10 shows five binarized image sequences from the two camera heads, with the  $x, y$  positions, velocities, and contours of the tracked egg cell, which were taken at intervals of 0.5 ms for  $t = 0.2480$ – $0.2520$  s. Figure 11 shows the changes in the eccentricity and velocity of the egg cell in the L-type microchannel. The velocities detected by our system were lower when the cell was close to the corner of the L-type micro-channel. By contrast, the eccentricity of the cell increased when the cell was close to the corner of the L-type micro-channel. The contours of cells could also be extracted at 1000 fps

by selecting small regions of interest (ROIs) in extracted bounding boxes of cells, which were extracted by hardware circuits.

The experimental results showed that the shape and movement of fast-flowing cells in an irregular microchannel could be quantified in real-time using our high-speed frame-straddling vision system.

## IV. CONCLUSION

In this study, we developed a rapid vision-based cell analysis system that quantified the shape and motions of cells simultaneously while flowing at 1 m/s or more in microchannels. Our system could extract the locations and shape features of multiple cells in two frame-straddled images in real time at 2000 fps or more by implementing multi-object moment feature extraction circuit modules on a dual-camera high-speed vision platform. This system obtained the velocities by setting a very small time delay between the two frame-straddled camera inputs, if their speed meant that they were too fast to track in a single-camera view. The experimental results showed that the shape deformations of sea urchin egg cells could also be quantified simultaneously, and this verified the performance of our system. Based on these results, we plan to improve our vision-based cell analysis system further so it can be used to inspect smaller cells, such as RBCs, in rapid microchannel flows. We also plan to develop an LOC-based cell-sorting system to manipulate fast-flowing cells in microchannels using simultaneous visual feedback control based on their shapes, motions, and other properties, as another step toward the automated mass production of good quality cells.

## REFERENCES

- [1] E. Oosterbroek and A. Van den Berg, Lab-on-a-chip: Miniaturized systems for (bio)chemical analysis and synthesis, Amsterdam: Elsevier, 2003.
- [2] Q.-Q. Ji, G.-S. Du, M. J. van Uden, Q. Fang, and J. M. den Toonder, "Microfluidic cytometer based on dual photodiode detection for cell size and deformability analysis," *Talanta*, vol. 111, pp. 178–182, 2013.
- [3] Z. Tong, E. M. Balzer, M. R. Dallas, W.-C. Hung, K. J. Stebe, and K. Konstantopoulos, "Chemotaxis of cell populations through confined spaces at single-cell resolution," *PLoS one*, vol. 7, no. 1, pp. e29211, 2012.
- [4] M. L. Heuzé, O. Collin, E. Terriac, A.-M. Lennon-Duménil, and M. Piel, "Cell migration in confinement: A micro-channel-based assay," *Cell Migration*, vol. 769, pp. 415–434, 2011.
- [5] A. M. Forsyth, J. Wan, W. D. Ristenpart, and H. A. Stone, "The dynamic behavior of chemically tiffened blood cells in microchannel flows," *Microvasc. Res.*, vol. 80, no. 1, pp. 37–43, 2010.
- [6] D. R. Gossett, H. T. K. Tse, S. A. Lee, Y. Ying, A. G. Lindgren, O. O. Yang, J. Rao, A. T. Clark, and D. Di Carlo, "Hydrodynamic stretching of single cells for large population mechanical phenotyping," *Proc. Natl. Acad. Sci.*, vol. 109, no. 20, pp. 7630–7635, 2012.
- [7] M. Kobatake, T. Takaki, and I. Ishii, "A real-time micro-PIV system using frame-straddling high-speed vision," in *Proc. IEEE Int. Conf. Robot. Automat.*, 2012, pp. 397–402.
- [8] Q. Gu, T. Takaki, and I. Ishii, "Fast FPGA-based multiobject feature extraction," *IEEE Trans. Circuits Syst. Video Technol.*, vol. 23, no. 1, pp. 30–45, 2013.
- [9] I. Ishii, T. Tatebe, Q. Gu, Y. Moriue, T. Takaki, and T. Tajima, "2000 fps real-time vision system with high-frame-rate video recording," in *Proc. IEEE Int. Conf. Robot. Automat.*, 2010, pp. 1536–1541.
- [10] Z. Zhang, "Flexible camera calibration by viewing a plane from unknown orientations," in *Proc. IEEE Int. Conf. Comput. Vis.*, vol. 1, 1999, pp. 666–673.
- [11] Q. Gu, T. Takaki, and I. Ishii, "A fast multi-object extraction algorithm based on cell-based connected components labeling," *IEICE Trans. Inform. Syst.*, vol. E95-D, no. 2, pp. 636–645, 2012.